

Infrared photovoltaic detectors⁺

A. ROGALSKI*

Institute of Applied Physics, Military University of Technology, Warsaw, Poland

At present efforts in infrared (IR) detector research are directed towards improving the performance of single element devices, large electronically scanned arrays and higher operating temperatures. Another important aim is to make IR detectors cheaper and more convenient to use. Investigations of the performance of narrow gap semiconductor photodiodes are presented. Recent progress in different IR photodiode technologies is discussed: HgCdTe photodiodes, InSb photodiodes, alternative to HgCdTe III-V and II-VI ternary alloy photodiodes, and lead chalcogenide photodiodes. Investigations of the performance of photodiodes operated at short wavelength IR (SWIR), 1–3 μm ; medium wavelength IR (MWIR), 3–5 μm ; and long wavelength IR (LWIR), 8–14 μm ; are presented.

The operating temperature for HgCdTe detectors is higher than for other types of photon detectors. HgCdTe detectors with background limited performance operate with thermoelectric coolers in the medium wavelength range, instead the long wavelength detectors operate at ≈ 100 K. HgCdTe is characterized by high absorption coefficient and quantum efficiency and relatively low thermal generation rate compared to other detectors.

1. Introduction

The years during World War II saw the origins of modern infrared detector technology. Recent success in applying infrared technology to remote sensing problems has been made possible by the successful development of high-performance IR detectors over the last five decades. Many materials have been investigated in the infrared field. Spectral detectivity curves for a number of commercially available IR detectors are shown in Fig. 1. Interest has centred mainly on the wavelengths of the two atmospheric windows 3–5 μm and 8–14 μm , though in recent years there has been increasing interest in longer wavelengths stimulated by space applications.

During the 1950s IR detectors were built using single-element-cooled lead salt detectors, primarily for anti-air-missile seekers. Usually lead salt detectors

were polycrystalline and were produced by vacuum evaporation and chemical deposition from a solution, followed by a post-growth sensitisation process [1]. The first extrinsic photoconductive detectors were reported in the early 1950s. Since the techniques for controlled impurity introduction became available for germanium at an earlier date, the first high performance extrinsic detectors were based on the use of germanium. Extrinsic photoconductive response from copper, zinc, and gold impurity levels in germanium made devices possible in the 8- to 14- μm long wavelength spectral window (LWIR) and beyond to the 14- to 30- μm very long wavelength region (VLWIR). The extrinsic photoconductors were widely used at wavelengths beyond 10 μm , prior to the development of the intrinsic detectors. They must be operated at lower temperatures to achieve performance similar to that of intrinsic detectors, and a sacrifice in

* corresponding author: A. Rogalski, Institute of Applied Physics, Military University of Technology, 2 Kaliski Str., 01-489 Warsaw, Poland

⁺ Presented at the 12th School of Optoelectronics: Photovoltaics – Solar Cells and Infrared Detectors, Kazimierz Dolny, May 22-24, 1997.

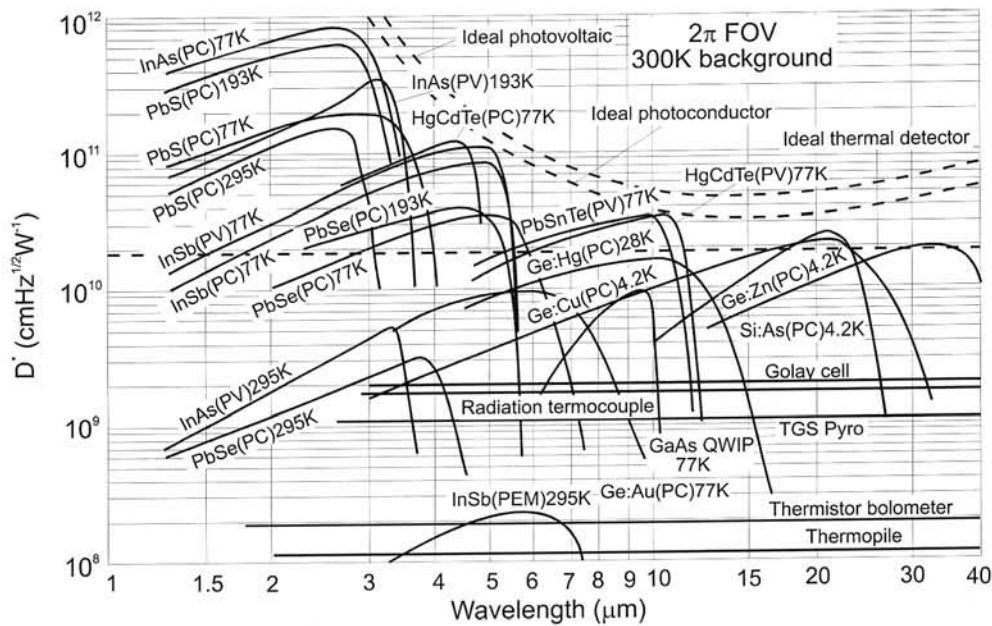


Fig. 1. Comparison of the D^* of various commercially available infrared detectors when operated at the indicated temperature. Chopping frequency is 1000 Hz for all detectors except the thermopile (10 Hz), thermocouple (10 Hz), thermistor bolometer (10 Hz), Golay cell (10 Hz) and pyroelectric detector (10 Hz). Each detector is assumed to view a hemispherical surround at a temperature of 300 K. Theoretical curves for the background-limited D^* for ideal photovoltaic and photoconductive detectors and thermal detectors are also shown.

quantum efficiency is required to avoid impractically thick detectors.

At the same time, rapid advances were being made in narrow bandgap semiconductors that would later prove useful in extending wavelength capabilities and improving sensitivity. The first such material was InSb, a member of the newly discovered III–V compound semiconductor family. The end of the 1950s saw the introduction of semiconductor alloys in III–V, IV–VI, and II–VI material systems. These alloys allowed the bandgap of the semiconductor and hence the spectral response of the

detector to be custom tailored for specific applications. In 1959, research by Lawson and co-workers triggered development of variable bandgap $\text{Hg}_{1-x}\text{Cd}_x\text{Te}$ (HgCdTe) alloys, providing an unprecedented degree of freedom on infrared detector design [2].

The performance of IR detectors is determined by fundamental physical properties of materials used for their fabrication. HgCdTe as the most important intrinsic semiconductor alloy systems for IR detectors is well established. The specific advantages of HgCdTe are the direct energy gap, ability to obtain both low and

Table 1. Some physical properties of narrow gap semiconductors.

Material	E_g (eV)		n_i (cm^{-3})		ϵ	μ_e ($10^4 \text{ cm}^2/\text{Vs}$)		μ_h ($10^4 \text{ cm}^2/\text{Vs}$)	
	77 K	300 K	77 K	300 K		77 K	300 K	77 K	300 K
InAs	0.414	0.359	6.5×10^3	9.3×10^{14}	14.5	8	3	0.07	0.02
InSb	0.228	0.18	2.6×10^9	1.9×10^{16}	17.9	100	8	1	0.08
$\text{In}_{0.53}\text{Ga}_{0.47}\text{As}$	0.66	0.75		5.4×10^{11}	14.6	7	1.38		0.05
PbS	0.31	0.42	3×10^7	1.0×10^{15}	172	1.5	0.05	1.5	0.06
PbSe	0.17	0.28	6×10^{11}	2.0×10^{16}	227	3	0.10	3	0.10
PbTe	0.22	0.31	1.5×10^{10}	1.5×10^{16}	428	3	0.17	2	0.08
$\text{Pb}_{1-x}\text{Sn}_x\text{Te}$	0.1	0.1	3.0×10^{13}	2.0×10^{16}	400	3	0.12	2	0.08
$\text{Hg}_{1-x}\text{Cd}_x\text{Te}$	0.1	0.1	3.2×10^{13}	2.3×10^{16}	18.0	20	1	0.044	0.01
$\text{Hg}_{1-x}\text{Cd}_x\text{Te}$	0.25	0.25	7.2×10^8	2.3×10^{15}	16.7	8	0.6	0.044	0.01

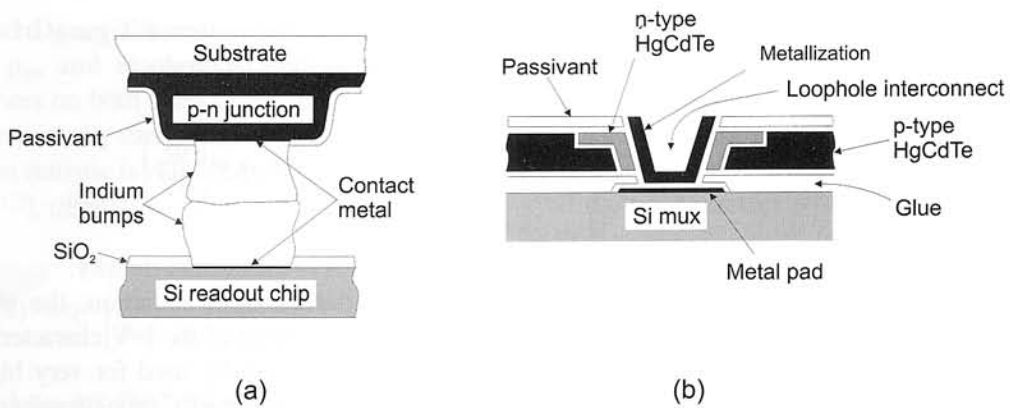


Fig. 2. Hybrid IR FPA interconnect techniques between a detector array and silicon multiplexer: (a) indium bump technique, (b) loophole technique (after Ref. 4).

high carrier concentrations, high mobility of electrons and low dielectric constant. The extremely small change of lattice constant with composition makes it possible to grow high quality layered and graded gap structures. HgCdTe can be used for detectors operated at various modes, and can be optimised for operation at the extremely wide range of the IR spectrum (1–30 μm) and at temperatures ranging from that of liquid helium to room temperature. HgCdTe has, however, the most serious technological problems of any semiconductor material in mass production. The difficulties with this material have made it desirable to examine other material systems to see whether performance can be improved. Table 1 listed important parameters of the materials used in IR detectors fabrication.

Several structures are possible to observe the photovoltaic effect. These include p–n junctions, heterojunctions, Schottky barriers and MIS photocapacitors. Each of these different types of devices has certain advantages for IR detection, depending on the particular application.³ Recently, more interest has been focused on the first two structures, so further considerations are restricted to p–n junctions and heterostructures. Photodiodes with their very low power dissipation and easy multiplexing on focal plane silicon chip, can be assembled in two-dimensional (2-D) arrays containing a very large ($\approx 10^6$) number of elements, limited only by existing technologies. Figure 2 shows the physical and electrical mating of a 2-D array of detectors to a silicon multiplexer, with individual interconnections between each detector and the corresponding input to the multiplexer. Systems based upon such focal plane arrays (FPAs) can be smaller, lighter with lower power consumption, and can result in much higher performance than systems based on first generation detectors. Photodiodes can also have less low frequency noise, faster response time, and the potential for a more uniform spatial response across each element. However,

the more complex processes needed for photovoltaic detectors have influenced on slower development and industrialisation of the second generation systems, particularly for large arrays.

2. Theory of p–n junction photodiode

The operation of the p–n junction photodiode is illustrated in Fig. 3. Photons with energy greater than the energy gap, incident on the front surface of the device, create electron-hole pairs in the material on both sides of the junction. By diffusion, the electrons and holes generated within a diffusion length from the junction reach the space-charge region. Then electron-hole pairs are separated by the strong electric field; minority carriers are readily accelerated to become majority carriers on the other side. This way a photocurrent is generated which shifts the current-voltage characteristic in the direction of negative or reverse current, as shown in Fig. 3(c). The equivalent circuit of a photodiode is shown in Fig. 3(b).

The total current density in the p–n junction is usually written as

$$J(V, \Phi) = J_d(V) - J_{ph}(\Phi) \quad (1)$$

where the dark current density, J_d , depends only on V and the photocurrent depends only on the photon flux density Φ .

Generally, the current gain in a simple photovoltaic detector (e.g., not in an avalanche photodiode) is equal to 1, and then the magnitude of photocurrent is given by

$$I_{ph} = \eta q A \Phi \quad (2)$$

where η is the quantum efficiency, q is the electron charge, and A is the detector area.

If the p–n diode is open-circuited, the accumulation of electrons and holes on the two sides of the junction

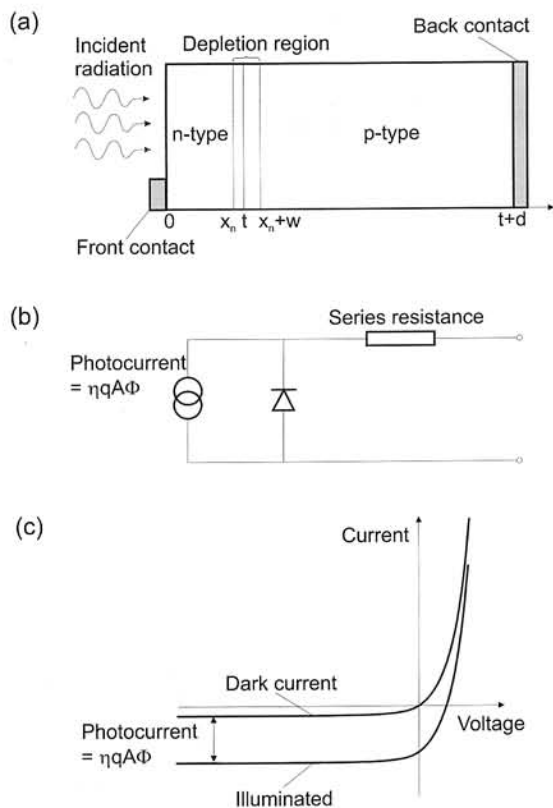


Fig. 3. Schematic representation of the operation of a p-n junction photodiode: (a) geometrical model of the structure, (b) equivalent circuit of an illuminated photodiode (the series resistance includes the contact resistance as well as the bulk p- and n-regions), (c) current-voltage characteristics for the illuminated and non-illuminated photodiode.

produces an open-circuit voltage [Fig. 3(c)]. If a load is connected to the diode, a current will conduct in the circuit. The maximum current is realised when an electrical short is placed across the diode terminals, and this is called the short-circuit current.

The open-circuit voltage can be obtained by multiplying the short-circuit current by the incremental diode resistance $R = (\delta I / \delta V)^{-1}$ at $V = V_b$:

$$V_{ph} = \eta q A \Phi R \quad (3)$$

where V_b is the bias voltage and $I = f(V)$ is the current-voltage characteristic of the diode.

In many direct applications the photodiode is operated at zero-bias voltage:

$$R_o = \left(\frac{\delta I}{\delta V} \right)^{-1} \bigg|_{V_b=0} \quad (4)$$

A frequently encountered figure of merit for a photodiode is the $R_o A$ product

$$R_o A = \left(\frac{\delta J}{\delta V} \right)^{-1} \bigg|_{V_b=0} \quad (5)$$

where $J = I/A$ is the current density.

In the detection of radiation, the photodiode is operated at any point of the I-V characteristic. Reverse bias operation is usually used for very high frequency applications to reduce the RC time constant of the devices.

The spectral current responsivity is equal to

$$R_i = \frac{\lambda \eta}{hc} qg \quad (6)$$

where λ is the wavelength, h is Planck's constant, and c is the light velocity.

Detectivity D^* is the main parameter characterising normalised signal to noise performance of detectors and can be defined as

$$D^* = \frac{R_i (A \Delta f)^{1/2}}{I_n} \quad (7)$$

where Δf is the frequency band.

2.1. Ideal diffusion-limited p-n junctions

Diffusion current is the fundamental current mechanism in a p-n junction photodiode. Figure 3(a) shows a one-dimensional photodiode model with an abrupt junction where the spatial charge of width w surrounds the metallographic junction boundary $x = t$, and two quasineutral regions $(0, x_n)$ and $(x_n + w, t + d)$ are homogeneously doped. The dark current density consists of electrons injected from the n-side over the potential barrier into the p-side and an analogous current due to holes injected from the p-side into the n-side. The current-voltage characteristic for an ideal diffusion-limited diode is given by

$$I_D = A J_s \left[\exp \left(\frac{qV}{kT} \right) - 1 \right] \quad (8)$$

where J_s is the saturation current density.

For a junction with thick quasineutral regions [$x_n \gg L_h$, $(t + d - x_n - w) \gg L_e$] the saturation current density is equal to

$$J_s = \frac{q D_h p_{no}}{L_h} + \frac{q D_e n_{po}}{L_e} \quad (9)$$

where D_e and D_h are the minority carrier diffusion coefficients, p_{no} and n_{po} are the concentrations of minority carriers on both sides of the junction; and L_e and L_h are the minority carrier diffusion lengths. When the Boltzmann statistic is valid [$n_o p_o = n_i^2$, $D = (kT/q)\mu$ and $L = (D\tau)^{1/2}$], then

$$J_s = (kT)^{1/2} n_i^2 q^{1/2} \left[\frac{1}{p_{po}} \left(\frac{\mu_e}{\tau_e} \right)^{1/2} + \frac{1}{n_{no}} \left(\frac{\mu_h}{\tau_h} \right)^{1/2} \right]^{-1} \quad (10)$$

where p_{po} and n_{no} are the hole and electron majority carrier concentrations, and τ_e and τ_h the electron and hole lifetimes in the p- and n-type regions, respectively. Diffusion current varies with temperature as n_i^2 .

The resistance at zero bias can be obtained from Eq. (8) by differentiation of I-V characteristic

$$R_o = \frac{kT}{qI_s} \quad (11)$$

and then the $R_o A$ product determined by diffusion current is:

$$(R_o A)_D = \left(\frac{dJ_D}{dV} \right)^{-1} \Big|_{V_b=0} = \frac{kT}{qJ_s} \quad (12)$$

For an n⁺-p diode structure, the junction resistance is limited by diffusion of minority carriers from the p side into the depletion region. In the case of conventional bulk diodes, where $d \gg L_e$:

$$(R_o A)_D = \frac{(kT)^{1/2}}{q^{1/2} n_i^2} N_a \left(\frac{\tau_e}{\mu_e} \right)^{1/2} \quad (13)$$

By thinning the substrate to a thickness smaller than the minority-carrier diffusion length (thus reducing the volume in which diffusion current is generated) the corresponding $R_o A$ product increases, provided that the back surface is properly passivated to reduce surface recombination. In the case of the n⁺-p junction, if the thickness of the p type region is such that $d \ll L_e$, we obtain:

$$(R_o A)_D = \frac{kT}{q^2} \frac{N_a}{n_i^2} \frac{\tau_e}{d} \quad (14)$$

As the result, $R_o A$ can increase by a factor of L_e/d . Of course, analogical formulae can be obtained for p⁺-n junctions.

Normally, the photodiode is designed so that most of the radiation is absorbed in one side of the junction, e.g., in the p-type side in Fig. 3(a). This could be

achieved in practice either by making the n-type region very thin or by using a heterojunction in which the band gap in the n-region is larger than the photon energy so that most of the incident radiation can reach the junction without being absorbed.

If the back contact is several minority carrier diffusion lengths, L_e , away from the junction, the quantum efficiency is given by

$$\eta(\lambda) = (1-r) \frac{\alpha(\lambda)L_e}{1 + \alpha(\lambda)L_e} \quad (15)$$

If the back contact is smaller than a diffusion length away from the junction, the quantum efficiency tends to

$$\eta(\lambda) = (1-r) [1 - e^{-\alpha(\lambda)d}] \quad (16)$$

where d is the thickness of the p-type region. It has been assumed that the back contact has zero surface recombination velocity and that no radiation is reflected from the back surface. Thus, if the above conditions hold, a high quantum efficiency can be achieved using an anti-reflection coating to minimise the reflectance of the front surface and ensuring that the device is thicker than the absorption length.

It can be shown, that the noise current of diode at zero bias voltage is equal [3]

$$I_n^2 = \frac{4kT\Delta f}{R} + 2q^2\eta A\Phi_b\Delta f \quad (17)$$

and the noise voltage

$$V_n = (4kT + 2q^2\eta A\Phi_b R_o) R_o \Delta f \quad (18)$$

The detectivity can be determined as

$$D^* = \frac{\eta\lambda q}{hc} \left[\frac{4kT}{R_o A} + 2q^2\eta\Phi_b \right]^{-1/2} \quad (19)$$

from Eqs. (6), (7) and (18).

For the last formula we may distinguish two important cases:

- background-limited performance; if $4kT/R_o A \ll 2q^2\eta\Phi_b$, then we obtain

$$D_b^* = \frac{\lambda}{hc} \left(\frac{\eta}{\Phi_b} \right)^{1/2} \quad (20)$$

- thermal noise limited performance; if $4kT/R_o A \gg 2q^2\eta\Phi_b$, then

$$D^* = \frac{\eta\lambda q}{2hc} \left(\frac{R_o A}{kT} \right)^{1/2} \quad (20)$$

2.2. Other current mechanisms

In the previous section, photodiodes were analysed in which the dark current was limited by diffusion. However, several additional excess mechanisms are involved in determining the dark current-voltage characteristics of the photodiode. The dark current is the superposition of current contributions from three diode regions: bulk, depletion region and surface.

Below, we will be concerned with the current contribution of high-quality photodiodes with high R_0A products limited by:

- generation-recombination within the depletion region,
- tunnelling through the depletion region,
- surface effects.

The first two mechanisms are schematically illustrated in Fig. 4.

The generation-recombination current of the depletion region can be described as

$$J_{GR} = \frac{qwn_i}{\tau_0} \quad (21)$$

if a trap is near the intrinsic level of the band gap energy. In this equation τ_0 is the carrier lifetime in depletion region. The surface leakage current can be described in the same way [3].

The comparison of equations (10) and (21) indicates that the space-charge region generation-recombination current varies with temperature as n_i , i.e., less rapidly than diffusion current which varies as n_i^2 .

The zero bias resistance can be found by differentiating Eq. (21) and setting $V = 0$:

$$(R_0A)_{GR} = \left(\frac{dJ_{GR}}{dV} \right)^{-1} \Big|_{V=0} = \frac{2V_b\tau_0}{qn_iw} \quad (22)$$

where $V_b = kT \ln(N_a N_d / n_i^2)$. In evaluating Eq. (22), the term of greatest uncertainty is τ_0 .

The third type of dark current component that can exist is a tunnelling current caused by electrons directly tunnelling across the junction from the valence band to the conduction band (direct tunnelling) or by electrons indirectly tunnelling across the junction by way of intermediate trap sites in the junction region (indirect tunnelling or trap-assisted tunnelling – see Fig. 4).

The tunnelling current (and R_0A product) is critically dependent on doping concentration. Fig. 5 shows the dependence of the R_0A product components on the dopant concentrations for one-sided abrupt HgCdTe, PbSnTe and PbSnSe photodiodes at 77 K ($E_g = 0.1$ eV). To produce high R_0A products for HgCdTe and lead salt photodiodes, the doping concentration of 10^{16} cm^{-3} and 10^{17} cm^{-3} (or less) are required, respectively. The maximum available doping levels due to onset of tunnelling are more than an order of magnitude higher with IV–VI than with HgCdTe photodiodes [6]. This is due to their high permittivities ϵ_s because tunnelling contribution of the R_0A product contains $\exp[\text{const}(m^*\epsilon_s / N)^{1/2}E_g]$ factor.

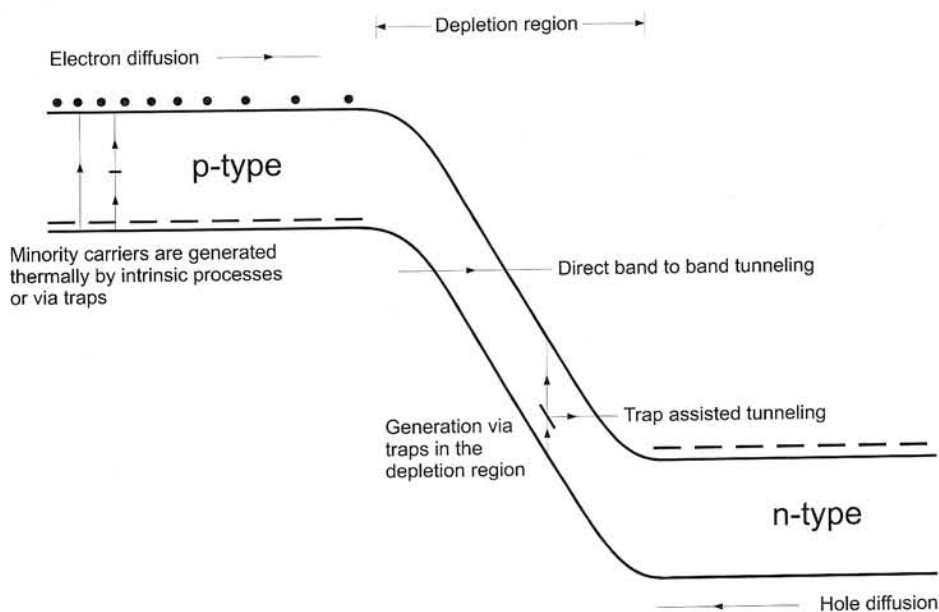


Fig. 4. Schematic representation of some of the mechanisms by which dark current is generated in a reverse biased p-n junction (after Ref. 5).

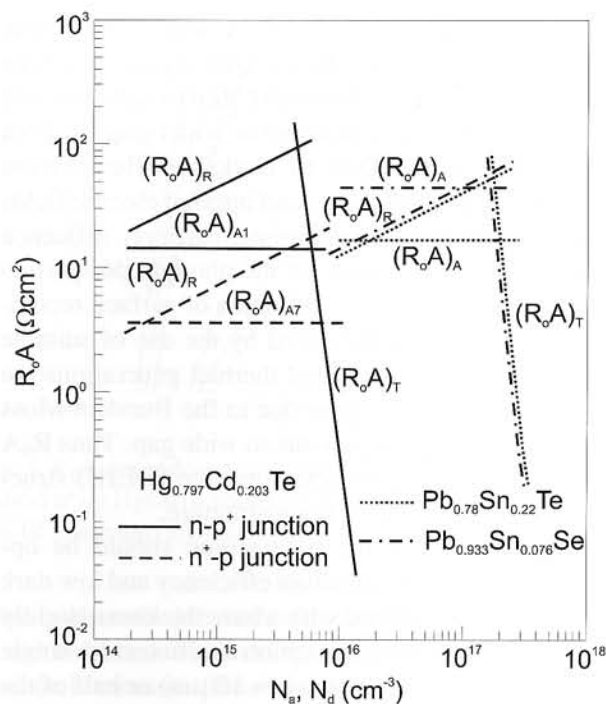


Fig. 5. The dependence of the R_oA product on doping concentration for one-sided abrupt HgCdTe, PbSnTe and PbSn-Se photodiodes at 77 K ($E_g = 0.1$ eV) (after Ref. 6).

3. InGaAs photodiodes

$\text{In}_{0.53}\text{Ga}_{0.47}\text{As}$ alloy lattice matched to the InP substrate has already been shown to be a suitable detector material for near-IR (1.0–1.7 μm) spectral range. InGaAs ternary alloy having lower dark current and noise than indirect-bandgap germanium, the competing near-IR material, the material is addressing both entrenched applications including low light level night vision (in the region 1–3 μm) and new applications such as remote sensing, eye-safe range finding and process control.

InGaAs-detector processing technology is similar to that used with silicon, but the detector fabrication is different. The InGaAs detector's active material is deposited onto a substrate using chloride VPE or MOCVD techniques adjusted for thickness, background doping, and other requirements. Planar technology evolved from the older mesa technology and at present is widely used due to its simple structure and processing as well as the high reliability and low cost [7, 8].

Figure 6 shows that the highest quality InGaAs photodiodes have been grown by MOCVD [9]. Their performance agrees with the radiative limit and is comparable with HgCdTe photodiodes.

Linear array formats of 256, 512 and 1024 elements have been fabricated for environmental sensing from

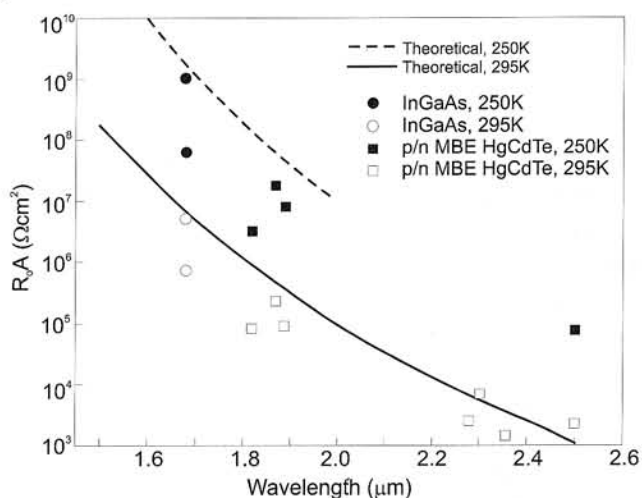


Fig. 6. Near IR and short wavelength IR detector R_oA vs. wavelength at 295 K and 250 K (after Ref. 9).

0.8 μm to 2.6 μm . The sizes of pixels are different; from $30 \times 30 \mu\text{m}^2$ (with spacing of 50 μm), $25 \times 500 \mu\text{m}^2$ to $13 \times 500 \mu\text{m}^2$ (with spacing of 25 μm). Sensors Unlimited offers $10 \times 10 \times 6$ -cm line-scan cameras incorporating linear InGaAs FPAs of up to 512 elements on a 50- μm pitch [10]. Two versions of the units are available, optimised for wavelength bands of either 0.8 to 1.7 μm or 1.0 to 2.2 μm .

The first two-dimensional 128×128 $\text{In}_{0.53}\text{Ga}_{0.47}\text{As}$ hybrid FPA for the 1.0–1.7 μm spectral range was demonstrated by Olsen et al. in 1990 [11]. Room-temperature measurements of a camera based on a 128×128 InGaAs FPA (with Rockwell's readout CMOS multiplexer) indicated that the mean value of D^* was $1.03 \times 10^{13} \text{ cmHz}^{1/2}\text{W}^{-1}$ with the standard deviation 45% of the mean and 94.8% of the pixels with a D^* greater than 50% of the mean value [12]. At 230 K the mean D^* was $3.5 \times 10^{14} \text{ cmHz}^{1/2}\text{W}^{-1}$.

4. InSb photodiodes

InSb photodiodes have been available since the late fifties and are generally fabricated by impurity diffusion, ion implantation, LPE, or MBE [3]. Wimmers et al. have presented the status of InSb photodiode technology for a wide variety of linear and FPAs [13, 14]. Fabrication techniques for InSb photodiodes use gaseous diffusion, and a subsequent etch results in a p-type mesa on n-type substrate with donor concentration about 10^{15} cm^{-3} .

Typical InSb photodiode RA product at 77 K is $2 \times 10^6 \Omega\text{cm}^2$ at zero bias and $5 \times 10^6 \Omega\text{cm}^2$ at slight reverse biases of approximately 100 mV. This charac-

teristic is beneficial when the detector is used in the capacitive discharge mode. As element size decreases below 10^{-4} cm^2 , some slight degradation in resistance due to surface leakage occurs.

InSb photovoltaic detectors are widely used for ground-based infrared astronomy and for applications aboard the Space Infrared Telescope Facility (SIRTF).

Recently, impressive progress has been made in the performance of InSb hybrid FPAs. The U.S. Naval Observatory and the National Optical Astronomy Observatories in collaboration with the Santa Barbara Research Center developed a 1024×1024 InSb FPA [15]. It is the largest single chip IR array in use today. The architecture of this device consists of four independent 512×512 quadrants with eight outputs per quadrant. An array of this size is only possible because the InSb detector material is thinned to less than $10 \text{ }\mu\text{m}$ which allows it to accommodate the InSb/silicon thermal mismatch.

InSb photodiodes can also be operated in the temperature range above 77 K . Of course, the RA products degrade in this region. At 120 K , RA products of $10^4 \text{ }\Omega\text{cm}^2$ are still achieved with slight reverse bias, making BLIP operation possible. The quantum efficiency in InSb photodiodes optimised for this temperature range remains unaffected up to 160 K [14].

5. HgCdTe photodiodes

Hitherto, the realisation of HgCdTe photodiodes has usually based on the most common n^+-p and p^+-n structure (symbol “+” denotes strong doping, underlined “_” wider gap). In such diodes, the lightly doped narrow gap absorbing region (“base” of the photo-

diode), determines the dark current and photocurrent. In these photodiodes the base p-type layers (or n-type layers) are sandwiched between CdZnTe substrate and high-doped (in n^+-p structures) or wider-gap (in p^+-n structure) regions. Due to backside illumination (through CdZnTe substrate) and internal electric fields (which are “blocking” for minority carriers), influence of surface recombinations on the photodiodes performance is eliminated. The influence of surface recombination can be also prevented by the use of suitable passivation. Both optical and thermal generations are suppressed in the n^+ -region due to the Burstein-Moss effect and in the p^+ -region due to wide gap. Thus R_0A product of double-layer heterojunction (DLHJ) structure is higher than that of homostructure.

The thickness of the base region should be optimised for near unity quantum efficiency and low dark current. This is achieved with a base thickness slightly higher than the inverse absorption coefficient for single pass devices: $t = 1/\alpha$ (which is $\approx 10 \text{ }\mu\text{m}$) or half of the $1/\alpha$ for double pass devices (devices supplied with a retroreflector). Low doping is beneficial for low thermal generation and high quantum efficiency.

A schematic of mesa DLHJ structure used in fabrication of p^+-n HgCdTe photodiodes together with its band diagram are illustrated in Fig. 7. The n-type base, which is the absorbing region, is deliberately doped with indium at a level of about $(1-3) \times 10^{15} \text{ cm}^{-3}$. The composition of the base material is chosen for the wavelength of interest. P-n junction is formed using arsenic as the dopant at a level of about 10^{18} cm^{-3} . P-type capping layers with composition $y > x$ have a thickness $1-2 \text{ }\mu\text{m}$. The electrical junction is positioned near the metallurgical interface and it is

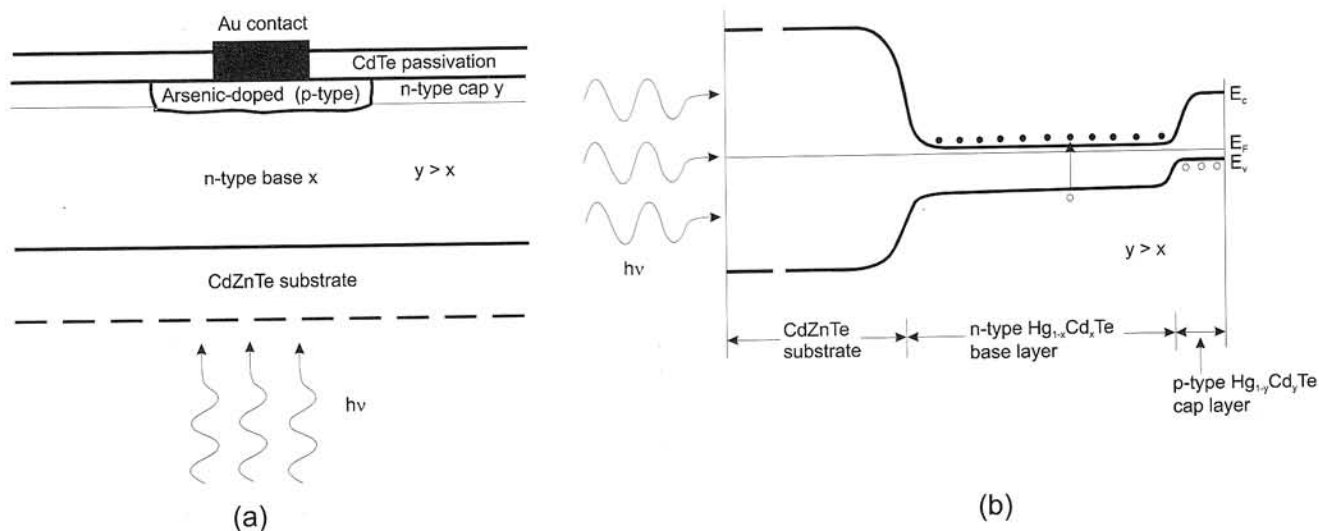


Fig. 7. DLHJ mesa p^+-n HgCdTe photodiode: (a) schematic cross-sectional view; (b) band diagram.

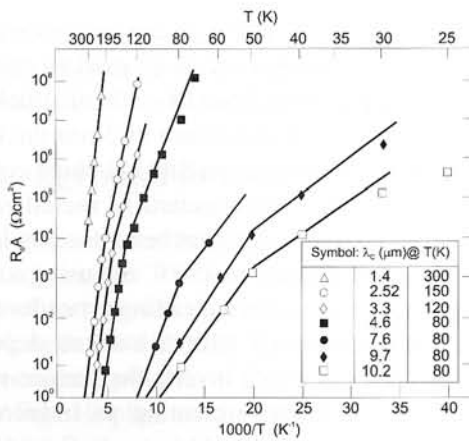


Fig. 8. R_oA dependence on reciprocal temperature for seven hybrid n^+-p HgCdTe photodiode arrays covering the 1–14- μm IR spectrum (after Ref. 19).

wise to place the junction in the small band gap layer to avoid deleterious effects on the quantum efficiency and dark currents. Passivation of HgCdTe has been done by several techniques which comprehensive review was given by Nemirovsky and Bahir [16]. Recently, however, most laboratories have been using CdTe or CdZnTe (deposited by MBE, MOCVD, sputtering and e-beam evaporation) for photodiode passivation [17].

Rogalski and Ciupa have compared the performance of n^+-p and p^+-n LWIR HgCdTe photodiodes [18]. It appears, that for the lowest doping levels achievable in controllable manner in the base regions of photodiodes ($N_a = 5 \times 10^{15} \text{ cm}^{-3}$ for n^+-p structure, and $N_d = 5 \times 10^{14} \text{ cm}^{-3}$ for p^+-n structure) the performance of both types of photodiodes is comparable for a given cutoff wavelength and temperature.

The temperature dependence of R_oA product of seven hybrid n^+-p photodiode arrays with different cut-off wavelengths is shown in Fig. 8. Note that the SWIR array is generation-recombination limited from room temperature to 120 K. The MWIR devices at $T < 150 \text{ K}$ are also dominated by generation-recombination current. The transition from diffusion to generation-recombination limited case is clearly seen in the LWIR arrays.

Usually, p-type base material is characterised by relatively high trap concentration, which dominates the excess carrier lifetime by the Shockley-Read-Hall recombination mechanism. Its influence depends on technological limits. However, the quality of p-type material has considerably improved in the last several years. Destefanis and Chamonal have developed a modified process for planar n^+-p HgCdTe homojunctions with a large improvement in detector perfor-

mance [20]. The n^+-p homojunctions were made by ion implantation in 8–12 μm thick HgCdTe liquid phase epilayers on CdZnTe substrates. The R_oA improvement of one order of magnitude (in the range between 400 to 650 Ωcm^2 at 77 K for a 10 μm cutoff wavelength detector) has been observed. This effect was obtained as a result of an increase of the minority carrier lifetime in the base p-type region (close to the Auger 7 limited lifetime) and a slightly thinner epitaxial p-type layer.

Up to the present, photovoltaic HgCdTe FPAs have been mainly based on p-type material. Linear (240, 288, 480, and 960 elements), 2-D scanning arrays with time delay and integration (TDI), and 2-D staring formats from 32×32 up to 1024×1024 have been made [9, 21–23]. Pixel sizes ranging from 18- μm square to over 1 mm have been demonstrated. The best results have been obtained using hybrid architecture, which permits independent optimisation of the materials parameters and device fabrication processes for detectors and the signal-processing electronics exploiting advances in a complementary metal-oxide-semiconductor (CMOS) fabrication processes.

6. Lead chalcogenide photodiodes

For a period of decade from the late 1960s to the mid 1970s, because of production and storage problems, HgCdTe alloy detectors were in serious competition with IV–VI alloy devices (mainly PbSnTe) for developing photodiodes [24, 25]. PbSnTe alloy seemed easier to prepare and appeared more stable. Development of PbSnTe photodiodes was discontinued because the chalcogenides suffered two significant drawbacks. The first one was a high dielectric constant that resulted in high diode capacitance and therefore limited frequency response. For scanning systems under development at that time, this was a serious limitation. However, for staring imaging systems under development today using 2-D arrays, this would not be as significant of an issue. The second drawback to IV–VI compounds is their very high thermal coefficients of expansion. This limited their applicability in hybrid configurations with silicon multiplexers. Today, with the ability to grow these materials on alternative substrates such as silicon, this too would not be a fundamental limitation. Moreover, as regards ease of manufacture, homogeneity and costs, photovoltaic IV–VI arrays on Si substrates offer substantial advantages compared to HgCdTe. The maximum available doping levels due to onset of tunnelling are more than an order of

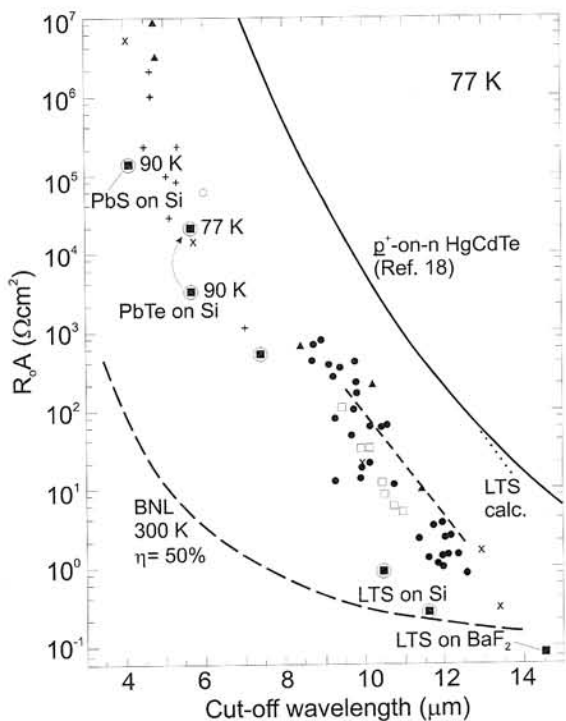


Fig. 9. R_0A products at 77 K versus cutoff wavelength for different lead salt photodiodes on Si with stacked BaF_2/CaF_2 or CaF_2 buffer layers. The BLIP limit for 300 K, 2π FOV and $\eta = 50\%$ is included (after Ref. 27). The solid line represents calculated and experimental data for p^+-n HgCdTe photodiodes according to Ref. 18.

magnitude higher with IV–VIs than with HgCdTe photodiodes (see Section 2).

To overcome thermal mismatch problems between

silicon readout substrate and lead chalcogenide detector for large arrays, Zogg *et al.* have used an epitaxial stacked CaF_2 – BaF_2 buffer layer of ≈ 200 nm thickness. The entire MBE growth procedure of 3 μ m thick lead chalcogenide epitaxial layer on Si(111) chips containing integrated circuits with standard Al metallizations has been performed [26]. This has been done by lowering the growth temperature to 450°C and using a room-temperature substrate surface cleaning procedure. The detectors were delineated with a vacuum-deposited blocking Pb contacts which inverts the surface region of p-type material, thereby creating an induced p-n junctions. A common ohmic contacts are formed with evaporated platinum.

Figure 9 shows R_0A products at 77 K as a function of cutoff wavelength for different lead salt photodiodes on Si with stacked BaF_2/CaF_2 and CaF_2 buffer layers.²⁷ Although these values are considerably above the BLIP limit (for 300 K, 2π FOV and $\eta = 50\%$), they are still significantly below theoretical limit given by Auger recombination. The performance of IV–VI photodiodes is inferior to HgCdTe photodiodes; their R_0A products are two orders of magnitude below values for p^+-n HgCdTe photodiodes. R_0A products of PbSnSe photodiodes with cutoff wavelength 10.5 μ m, were about 1 Ωcm^2 at 77 K. The temperature dependence of R_0A is diffusion limited down to 100 K, while depletion-limited noise dominates below this temperature.

The research group at the Swiss Federal Institute of Technology fabricated linear lead chalcogenide photodiode sensor monolithic arrays with 2×128

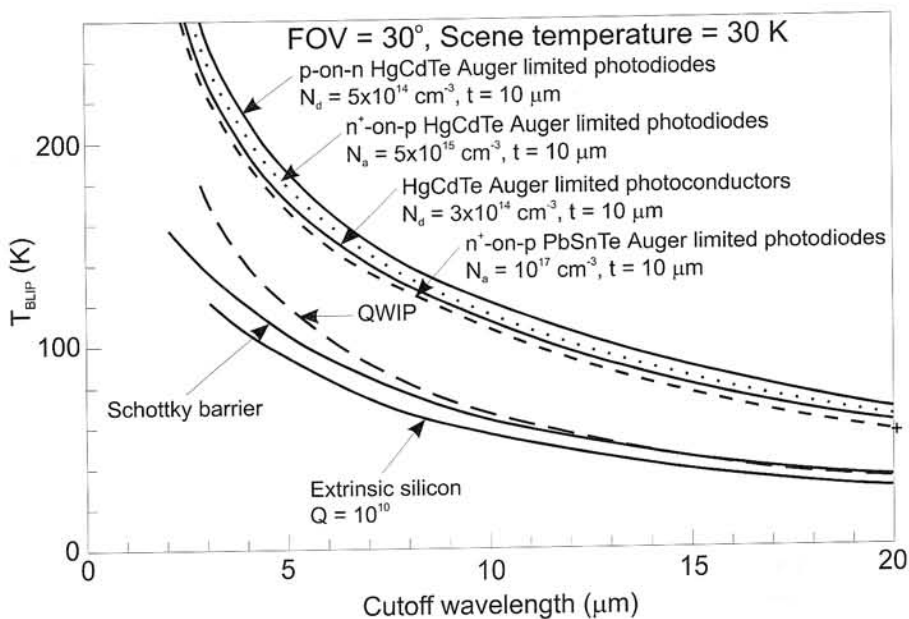


Fig. 10. Estimation of the temperature required for background limited operation of different types of photon detectors. In the calculations $FOV = 30^\circ$ and $T_B = 300$ K are assumed (after Ref. 28).

pixels and with cutoff wavelengths ranging from 3 to 12 μm , which have been used in one-direction mechanically scanned thermal imaging camera [27].

7. Background limited operation

In this section the temperature TBLIP required for background limited (BLIP) operation in 30° field of view (FOV) as a function of cutoff wavelength for different types of infrared photodetectors is analysed.

In Fig. 10 plots of the calculated temperature required for background limited (BLIP) operation in 30° FOV are shown as a function of cutoff wavelength. We can see that the operating temperature of "bulk" intrinsic IR detectors (HgCdTe and PbSnTe) is higher than for other types of photon detectors. HgCdTe detectors with background limited performance operate with thermoelectric coolers in the MWIR range, instead the LWIR detectors ($8 \leq \lambda_c \leq 12 \mu\text{m}$) operate at $\approx 100 \text{ K}$. HgCdTe is characterised by high optical absorption coefficient and quantum efficiency and relatively low thermal generation rate compared to extrinsic detectors, silicide Schottky barriers and quantum well IR photodetectors (QWIPs).

Conclusions

To summarize, despite serious competition from alternative technologies and slower progress than expected, HgCdTe is unlikely to be seriously challenged for high-performance applications, applications requiring multispectral capability and fast response. The recent successes of competing cryogenically cooled detectors are due to technological, not fundamental issues. There are good reasons to think that the steady progress in epitaxial technology would make HgCdTe devices much more affordable in the near future. The much higher operation temperature of HgCdTe compared to Schottky barrier devices and low-dimensional solid devices may become a decisive argument in this case. In applications for short-range thermal imaging systems a serious challenge comes from solid state arrays of thermal detectors (pyroelectric and bolometers) which are expected to take over and increase the market for uncooled short-range imaging systems.

References

- 1 R. J. Cushman: *Film-type infrared photoconductors*. Proc. IRE **47** (1959) 1471.
- 2 W. D. Lawson, S. Nielson, E. H. Putley and A. S. Young: *Preparation and properties of HgTe and mixed crystals of HgTe-CdTe*. J. Phys. Chem. Solids **9** (1959) 325.
- 3 A. Rogalski (Editor): *Infrared Photon Detectors*, SPIE Optical Engineering Press, Bellingham (1995).
- 4 D. A. Scribner, M. R. Kruer and J. M. Killiany: *Infrared focal plane array technology*. Proc. IEEE **79** (1991) 66.
- 5 C. T. Elliott and N. T. Gordon: Infrared detectors, in *Handbook on Semiconductors*, Vol. 4, pp. 841–936, edited by C. Hilsum, North-Holland, Amsterdam (1993).
- 6 A. Rogalski and W. Larkowski: *Comparison of photodiodes for the 3–5.5 μm and 8–14 μm spectral regions*. Electron Technology **18**(3/4) (1985) 55.
- 7 M. J. Cohen and G. H. Osen: *Near-IR imaging cameras operate at room temperature*. Laser Focus World (1993) 109.
- 8 G. H. Olsen, M. J. Lange, M. J. Cohen, D. S. Kim and S. R. Forrest: *Three-band 1.0–2.5 μm near-infrared InGaAs detector array*. Proc. SPIE **2235** (1994) 151.
- 9 L. J. Kozlowski, K. Vural, J. M. Arias, W. E. Tennant and R. E. DeWames: *Performance of HgCdTe, InGaAs and quantum well GaAs/AlGaAs staring infrared focal plane arrays*. Proc. SPIE **3182** (1997) 2.
- 10 M. J. Cohen and G. H. Olsen: *Near-infrared camera inspects with clarity*. Laser Focus World (June 1996) 269.
- 11 G. Olsen, A. Joshi, M. Lange, K. Woodruff, E. Mykietyn, D. Gay, G. Erickson, D. Ackley, V. Ban and C. Staller: *A 128 \times 128 InGaAs detector array for 1.0–1.7 microns*. Proc. SPIE **1341** (1990) 432.
- 12 M. J. Cohen and G. H. Olsen: *Room temperature InGaAs camera for NIR imaging*. Proc. SPIE **1946** (1993) 436.
- 13 J. T. Wimmers and D. S. Smith: *Characteristics of InSb photovoltaic detectors at 77 K and below*. Proc. SPIE **364** (1983) 123.
- 14 J. T. Wimmers, R. M. Davis, C. A. Niblack and D. S. Smit: *Indium antimonide detector technology at Cincinnati Electronics Corporation*. Proc. SPIE **930** (1988) 125.
- 15 A. M. Fowler, J. B. Heynssens, I. Gatley, F. J. Vrba, H. D. Ables, A. Hoffman and J. Woolaway: *ALADDIN, the 1024 \times 1024 InSb array: Test results*. Proc. SPIE **2475** (1995) 27.

- 16 Y. Nemirovsky and G. Bahir: *Passivation of mercury cadmium telluride surfaces*. J. Vac. Sci. Technol. **A7** (1989) 450.
- 17 W. E. Tennant, C. A. Cockrum, J. B. Gilpin, M. A. Kinch, M. B. Reine and R. P. Ruth: *Key issues in HgCdTe-based focal plane arrays: a industry perspective*. J. Vac. Sci. Technol. **B10** (1992) 1359.
- 18 A. Rogalski and R. Ciupa: *Long wavelength HgCdTe photodiodes: n^+ -on- p versus p -on- n structures*. J. Appl. Phys. **77** (1995) 3505.
- 19 M. Lanir and K. J. Riley: *Performance of PV HgCdTe arrays for 1–14 μm applications*. IEEE Trans. Electron Devices **ED29** (1982) 274.
- 20 G. Destefanis and F. P. Chamonal: *Large improvement in HgCdTe photovoltaic detector performances at LETI*. J. Electr. Mater. **22** (1993) 1027.
- 21 P. R. Norton: *Infrared image sensors*. Opt. Eng. **30** (1991) 1649.
- 22 R. E. DeWames, J. M. Arias, L. J. Kozlowski and G. M. Williams: *An assessment of HgCdTe and GaAs/GaAlAs technologies for LWIR infrared imagers*. Proc. SPIE **1735** (1992) 2.
- 23 L. J. Kozlowski, J. M. Arias, W. E. Tennant: *Experimental comparison of staring IR sensor technologies PV HgCdTe, PV InGaAs and quantum well GaAs/AlGaAs*. Proc. SPIE, to be published.
- 24 I. Melngailis and T. C. Herman: *Single-crystal lead-tin chalcogenides*, in *Semiconductors and Semimetals*, Vol. 5, pp. 111–174, edited by R. K. Willardson and A. C. Beer, Academic Press, New York (1970).
- 25 T. C. Harman and I. Melngailis: *Narrow gap semiconductors*, in *Applied Solid State Science*, Vol. 4, pp. 1–94, edited by R. Wolfe, Academic Press, New York (1974).
- 26 T. Hoshino, C. Maissen, H. Zogg, J. Masek, S. Blunier, A. N. Tiwari, S. Teodoropol and W. J. Bober: *Monolithic PbSnSe infrared sensor arrays on Si prepared by low-temperature process*. Infrared Physics **32** (1991) 169.
- 27 H. Zogg, A. Fach, C. Maissen, J. Masek and S. Blunier: *Photovoltaic lead-chalcogenide on silicon infrared sensor arrays*. Opt. Eng. **33** (1994) 1440.
- 28 A. Rogalski: *Comparison of the performance of quantum well and conventional bulk infrared photodetectors*. Infrared Phys. Technol. **38** (1997) 295.